

## Research Paper

# Diffused arching in embankments supported by non-compliant columns with capping beams

Karol Brzeziński<sup>a</sup>, Radoslaw L. Michalowski<sup>b,\*</sup>

<sup>a</sup> Faculty of Civil Engineering, Warsaw University of Technology, Warsaw, Poland, and Dekaban Fellow in the College of Engineering, University of Michigan, USA

<sup>b</sup> Department of Civil and Environmental Engineering, University of Michigan, 2028 GG Brown Bldg., 2350 Hayward, Ann Arbor, MI 48109-2125, USA

## ARTICLE INFO

## Keywords:

Diffused arching  
Piled embankments  
Efficacy  
Stress distribution  
Finite element analysis

## ABSTRACT

A column-supporting system for embankments on soft soils is analyzed using the Finite Element Method. The numerical problem has boundary conditions similar to that of a trap-door, but, contrary to the classical trap-door studies, the focus in this paper is on the load transfer to the supporting columns measured by the system efficacy, and on the critical embankment height that prevents differential settlements on the embankment surface. The stress state simulated in the embankment rapidly evolves in the first stages of the soft soil settlement, measured by millimeters, but the changes to the elastic–plastic stress field developed are marginal in the subsequent stages of settlement simulated up to 10 cm. The displacement field in low embankments with a height comparable to the column spacing is dominated by the failure mechanism with shear bands reaching the embankment crown, causing differential settlements on the embankment surface. In higher embankments, the failure mechanism is confined to the lower portion of the fill, and no differential settlements were detected on the embankment surface. It was suggested that a hypothetical *diffused* soil arch formed above the failure mechanism, with a shape approximately following the principal stress trajectories. This conjecture was made based on the presence of elevated stress along the symmetry plane of the embankment-column periodic cell. Numbers related to system efficacy and critical height are reported for a limited set of model parameters, but the qualitative outcome of the study is likely applicable to a wider variety of embankments.

## 1. Introduction

The authors dedicate this paper to the late Professor Gyan Pande, who was the co-founder of this Journal and its first Editor since its inception in 1985, and later continued as Co-Editor until 2010. The senior author of this paper met Professor Pande in the late 1980s at the Third Symposium on Numerical Models in Geomechanics (NUMOG) in Niagara Falls, Ontario. Since then, he met regularly with Prof. Pande, most notably at the memorable NUMOG Symposia, which Prof. Pande co-organized to the delight of the international geomechanics community, and, after the 10th NUMOG on the island of Rhodes, at the Computational Geomechanics (ComGeo) meetings, with the last one in the beautiful town of Assisi, Italy, in 2018. Professor Pande was a professional colleague and a friend, who over the years inspired many of those who met him. He will be missed by all of us.

Arching in soils is an elusive phenomenon that has not yet found a unique definition or comprehensive description in the technical literature. This is because, contrary to failure in soils where the process is distinctly visualized by its kinematics, arching is driven by varied

stiffness in structural support and it is manifested in the distinct distribution of stresses, not displacements. The less compliant support will carry the greater portion of the load. In the context of granular materials, this phenomenon is demonstrated in Fig. 1. The prismatic mound of sand is simulated using the Distinct Element Method (Nadukuru and Michalowski, 2012) and arching is caused by the non-uniform but linear settlement of the supporting surface; the settlement is the largest beneath the center of the mound and zero at the left and right extreme points. Arching is demonstrated by the shape of the strong force chains and by the distribution of the vertical reaction stress underneath the prism (Fig. 1). The settlement of the mound was caused by rotation of each half of the supporting base by  $0.05^\circ$  about the extreme left and right points. The reaction distribution after the settlement of the mound has a distinct local minimum underneath the center. This minimum indicates the load being transferred away from the center to the portions of the base with lesser settlement (less compliant). This type of reaction distribution can be caused by differential settlement of the base, as in the example discussed, but it also can be an outcome of the process of forming the prism (Michalowski and Park, 2004).

\* Corresponding author.

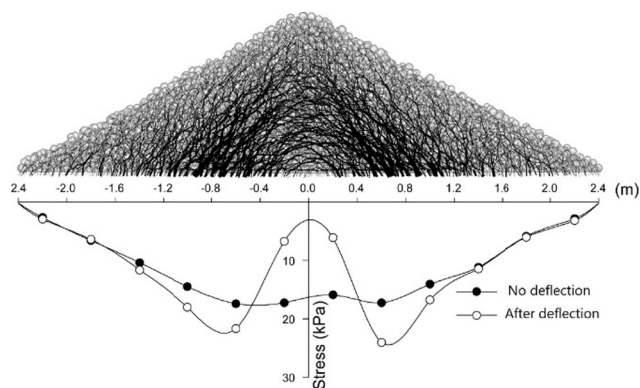


Fig. 1. Arching in a prismatic mound of sand simulated using distinct element method (modified from Nadukuru and Michalowski, 2012).

Arch formation in granular media is different from an architectural arch in that, contrary to Roman or gothic arches, an arch in sand requires some supporting stress along the lower contour. This is because granular materials, such as sand, have no strength against uniaxial compression, while the stress state along the contour of a structural arch is one-dimensional compression.

Arching is often mentioned in the context of flow of granular materials through silos and hoppers (Janssen, 1895, Drescher, 1991). While the phenomenon is beneficial in problems such as piled embankments on soft soils, arching is an impediment to the flow of bulk materials in storage containers, where it interferes with discharge of the granular medium (*jamming*). It is a common occurrence in operation of storage containers that moisture, or traces of oil from stored grain, may introduce a minute bonding between grains or particles, leading to minute one-dimensional compressive strength, just enough to cause arching and interruption of the technological process (Michalowski, 1984, Drescher, 1991). Terzaghi devoted a short chapter to soil arching in his book (Terzaghi, 1943), though, while explaining the phenomenon, he put more emphasis on soil failure in a trap-door problem (forming of a mechanism), rather than the development of an actual soil arch.

This paper's focus is on the development of the load transfer from an embankment to a column-support system, and the consequences on the system efficacy and the critical height of the embankment. The latter is defined as the minimum embankment height when the differential settlement does not propagate to the embankment surface. A brief commentary on the construction and design is given in the next section, followed by the finite element analysis in order to find the displacement increments, associated shear strain increments, and the principal stress trajectories. The boundary value problem in the numerical analysis is defined in a manner similar to that of the classical trap-door exercise (Terzaghi, 1943, Ladanyi and Hoyaux, 1969, Vardoulakis et al., 1981). The paper reports on some observations in the development of the displacement and shear strain incremental fields, offers some numerical results in terms of differential settlements and efficacy of the pile-support system, and provides comments on what might be considered soil arching.

## 2. Pile-supported embankments over soft soils

Development of transportation infrastructure often requires construction of roads through areas with relatively young, normally consolidated clay deposits and organic soils. Often considered marginal, construction of embankments over such soils may require a time-consuming solution where the soft deposits are consolidated prior to construction. An alternative and faster solution is providing a support system that allows transferring the embankment load to deeper, more competent deposits, with only a small portion of the load transferred to the soft soil. Pile- or column-supported embankments above soft soils

have been constructed for decades (Reid and Buchanan, 1984, Hewlett and Randolph, 1988, Poulos, 1998). While an effective way in construction, not all aspects of pile-support systems are fully understood.

There are at least two trends in the literature related to pile- or column-supported embankments. One has focused on the practical aspects of pile support systems, with the development of fairly simple, though often effective methods for design (for example, Low et al., 1994, Abusharar et al., 2009, Filz et al., 2012, Van Eekelen et al., 2013). The second trend is concentrated more on better understanding of the pile-support systems. Modern design methods include a layer above the columns, typically referred to as the *load transfer platform* (LTP), and often reinforced with a geogrid (Han and Gabr, 2002, Van Eekelen et al., 2013; Michalowski et al., 2018). The role of the LTP is to aid in the load transfer from the embankment to the piles or columns and, to some extent, mitigate differential settlements. However, even more important in the load transfer process is the formation of arching within the granular soil that extends through the LTP into the body of the embankment.

The phenomenon of soil arching is accounted for in design using practical observations and analytical methods with significant simplifying assumptions. It was the subject of a recent study by King et al. (2019). In that study, small physical models were constructed and the process of load transfer to the piles was simulated by increasing displacement (settlement) of soil between the supporting piles. Observations of failure kinematics were carried out using Synchrotron X-ray computed tomography. While this technique today allows only small models to be tested (the diameter of the model constructed did not exceed 15 cm), an interesting, but not unexpected mechanism of failure was detected. The technique is less effective when used to trace the development of soil arching, because arching is not manifested in the failure kinematics; rather, it is the stress distribution in embankments that reveals the features of soil arch formation.

In a recent case study where embankment serviceability failure was analyzed (Michalowski et al., 2018), it was an interruption of arch formation within the embankment soil that was found to be a likely cause of undesirable performance. Results of a finite element study are described in this paper in order to gain more understanding of how soil arch formation might progress in a column-supported embankment as a result of increasing settlement of the soft soil beneath.

## 3. Analysis of support system with capping beams on non-compliant columns

### 3.1. Problem statement

A schematic of a soil arch formation in a granular medium above a column-supporting system is illustrated in Fig. 2. Columns are capped with beams and soil arches are expected to extend between the neighboring beams. The soft soil between the capped rows of columns is expected to settle, thus the schematic in Fig. 2 can be interpreted as a system of periodic trap doors. The problem of soil failure associated with an individual trap door has a long history in the literature (e.g.,

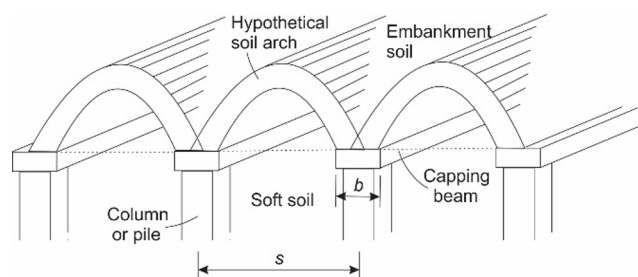


Fig. 2. Schematic of column support system with capping beams and sketch of presumed arch formation.

Terzaghi, 1943, Ladanyi and Hoyaux, 1969, Vardoulakis et al., 1981). The focus in this paper, however, is not on the mechanism of failure, but rather on the distribution of loads to determine the fraction of the embankment fill load that is carried by the capping beams. The interest in the kinematics is in defining the height of the embankment fill that would prevent the differential soil settlements occurring at the level immediately above the capping beams from propagating to the crown of the embankment. Such height will be referred to as the *critical height* of the embankment.

Because of equally spaced rows of columns, a periodic cell is defined that extends from the center of one row of columns to the center of the neighboring row, as indicated by spacing  $s$  in Fig. 2. Because of the presumed symmetry of arch formation between two neighboring capping beams, a symmetric half of an individual cell was chosen for the numerical model, with boundary conditions defined in Fig. 3. The column spacing is denoted by  $s$ ,  $b$  is the width of the capping beam, and  $H$  is the embankment height.

The soft soil is not modeled, but its settlement is simulated by uniform downward displacement of the rigid plate shown in Fig. 3. It is recognized that the settlement of soft soil may not be uniform, but the influence of this uniformity will not be addressed in this paper. Because of the large length of the capping beams, the problem is formulated as a plane strain problem.

The embankment soil is modeled as elastic-perfectly plastic. This is a simple model that does not address the complexities of the soil behavior, for example those related to softening or stiffness evolution. The model, however, is expected to indicate the tendencies in efficacy of the pile support system and, to some extent, trends in embankment critical height. Practical approaches to design of pile support systems over soft soils are typically based on a rigid-body mechanics approach to formation of a soil arch. The approach proposed in this paper is expected to illuminate some aspects of arch formation in soils, as well as a possible failure pattern in the lower portion of the embankment, which might be helpful in assessing the tools used in practice.

Prior to reaching the limit state, the soil is considered to be governed by the isotropic Hooke's law, expressed in terms of Young's modulus  $E$  and Poisson's ratio  $\nu$ . The limit state of the embankment soil is described by Mohr-Coulomb function  $f(q,p) = 0$ , represented here in terms of stress invariants

$$f = R_{mc}q - p \tan \phi - c = 0 \tag{1}$$

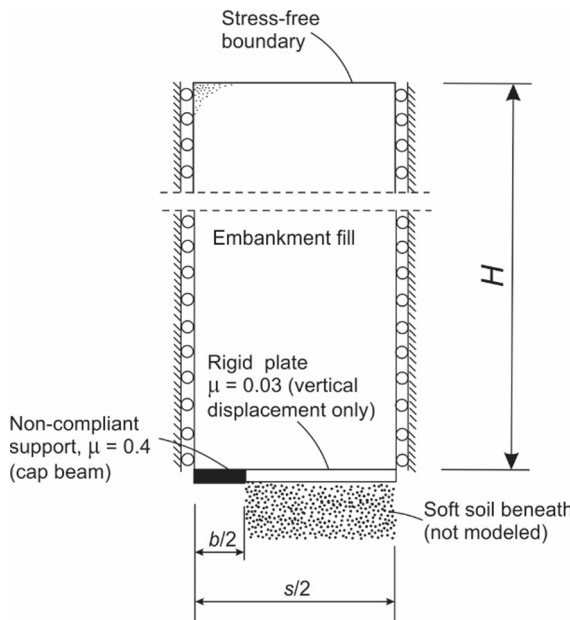


Fig. 3. Problem definition.

with  $\phi$  and  $c$  being material properties (internal friction angle and cohesion), and  $q$  and  $p$  are the variables dependent on the second invariant of the stress deviator,  $J_2$ , and the first invariant of the stress tensor  $I_1$

$$q = \sqrt{3J_2}, \quad p = -I_1/3 \tag{2}$$

and

$$R_{mc} = \frac{1}{\sqrt{3} \cos \phi} \sin(\theta + \frac{\pi}{3}) + \frac{1}{3} \cos(\theta + \frac{\pi}{3}) \tan \phi \tag{3}$$

with Lode angle  $\theta$  defined by

$$\cos(3\theta) = \frac{3\sqrt{3}}{2} \frac{J_3}{J_2^{3/2}} \tag{4}$$

where  $J_3$  is the third invariant of the deviatoric stress tensor. The plastic flow is assumed non-associative

$$\dot{\epsilon}_{ij}^{pl} = \dot{\lambda} \frac{\partial g(\sigma_{ij})}{\partial \sigma_{ij}} \tag{5}$$

with the plastic potential  $g(\sigma_{ij})$  defined by Menetrey and Willam (1995)

$$g = \sqrt{(\epsilon \tan \psi)^2 + (R_{mv} q)^2} - p \tan \psi \tag{6}$$

where  $\psi$  is the dilatancy angle,  $\epsilon$  is the "meridional eccentricity" (Abaqus 2011), and

$$R_{mv} = \frac{4(1 - e^2) \cos^2 \theta + (2e - 1)^2}{2(1 - e^2) \cos \theta + (2e - 1) \sqrt{4(1 - e^2) \cos^2 \theta + 5e^2 - 4e}} \frac{3 - \sin \phi}{6 \cos \phi} \tag{7}$$

with  $e$  termed a deviatoric eccentricity defined as

$$e = \frac{3 - \sin \phi}{3 + \sin \phi} \tag{8}$$

The basic set of both elastic and plastic properties used in the majority of computations is given in Table 1. Friction coefficients  $\mu$  between the pile cap beam and the embankment soil and between the plate (simulating the settlement of the soft soil beneath) and the embankment soil were taken as 0.4 and 0.03, respectively. Although the embankment fill is considered a granular soil with no bonding, a minute cohesion of 0.01 kPa was assumed to avoid numerical issues.

The embankment construction process is assumed to be *rapid*, and the settlement of the soft soil below the embankment during its construction is neglected. The model is built up by placing the soil in the cell and "switching" gravity on simultaneously in the entire embankment. The settlement of the soft soil below the embankment is then simulated by applying a series of 1-mm vertical displacement increments of the rigid plate, Fig. 3. Because the embankment soil is not sensitive to the rate of loading, the time-dependency of the plate settlement, caused by presumed consolidation of the soft soil beneath, was ignored.

To assess whether the assumption of rapid construction has a substantial influence on the results, an example is shown in Section 4.2 where the construction of the embankment is carried out in layers. The calculated efficacy of the system was found to be nearly identical to that found for rapid construction.

Table 1  
Material properties of the model.

$\rho$ (kg/m <sup>3</sup> )	$E$ (MPa)	$\nu$ -	$\phi$ (°)	$\psi$ (°)
1900	60	0.3	40	10.0

### 3.2. Finite element simulation of embankments with different heights

The geometry of the problem is defined by spacing of columns  $s = 2.0$  m, embankment height  $H$ , ranging from 1.0 to 5.0 m, and the capping beams' width  $b = 0.40$  m. Material properties of the embankment soil are given in Table 1. Vertical displacement of the rigid plate (Fig. 3), simulating the soft soil settlement, is applied in 1-mm increments. FEM system Abaqus (Abaqus, 2011) was used to simulate the problem. A regular finite element mesh was used with quadrilateral elements, quadratic shape functions, and reduced integration (CPE8R element type in Abaqus). The size of an individual element was 83 mm. Although tensile-positive sign convention is used in Abaqus, the results will be interpreted with compressive stresses as positive, consistent with the sign convention in geotechnical engineering. Consequently, the larger compressive principal stress will be referred to as the major principal stress.

First, vertical increments of displacement within the embankment soil are illustrated in Fig. 4 for a one-meter tall embankment and plate displacements  $\delta$  of 1, 2, 4, 6, and 20 mm. The color scale in the upper row, Fig. 4(a) through (e), indicates the magnitude of the vertical displacement increment. The maximum displacement increment in each graph, marked in dark red, is equal to the displacement increment of the plate (simulating the settlement of the soft soil), and is equal to 1 mm for each of Fig. 4(a) through (e). This will also be the case for the subsequent plots with results for embankments with different heights. The intensity of the maximum shear strain increment is shown in the lower row in Fig. 4(f) through (j). It is interesting to notice that the trapezoidal region that moved downward approximately as rigid with a displacement of 1.0 mm formed within the first 1-mm increment of the process. This mechanism is associated with the formation of a shear band that propagated nearly vertically from the edge of the capping beam to the embankment crown, Fig. 4(f), with soil above the cap beam hardly moving Fig. 4(a). Subsequently, the shear band leaned to the right, Fig. 4 (g) through (j), which is also reflected in the gradient of the vertical displacement increments in the first row of Fig. 4. The kinematics are dominated by the plastic mechanism reaching the crown of the embankment.

The black lines are the trajectories of the major principal stress; they were not smoothed by the algorithm used for plotting. Calculations with smaller increments of the plate displacement indicated that initially vertical trajectories quickly diverted to the right in the upper portion of the embankment fill to reach the right boundary (symmetry plane of the periodic cell). The major principal stress directions remain vertical in the lower portion of the fill, but they divert to the right, merging with the trajectory above. Although the upper trajectories assume an arch-like shape, no soil arch is formed as the kinematics are dominated by the failure mechanism reaching the embankment crown, clearly outlined by the vertical displacement increments in the upper row of plots in Fig. 4. This mechanism persists beyond the 20-mm settlement of the soft soil.

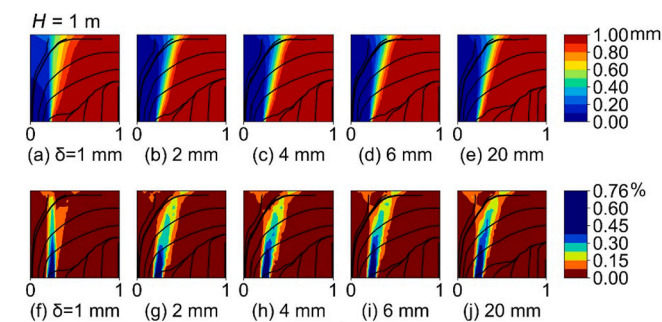


Fig. 4. Embankment with 1-m height at  $\delta = 1, 2, 4, 6,$  and  $20$  mm: (a) – (e) a sequence of vertical displacement increments, and (f) – (j) a sequence of maximum shear strain increments ( $s = 2.0$  m,  $b = 0.4$  m).

In the simulation presented in Fig. 4 and throughout the paper, bands of localized strain were detected during the deformation process. The conventional displacement-based formulation was adopted in the FEM approach without any regularization technique typically used to avoid the known dependence of the computational outcome on the mesh size. Instead, the mesh-sensitivity of the results was analyzed through simulations with varied mesh sizes. Observations of the deformation field did not reveal any significant mesh-dependency on its character (pattern of shear bands), but the magnitude of calculated efficacy of the system changed by a small amount, reported in Section 4.2.

A series of displacement and maximum shear strain increments for a 2-m embankment is illustrated in Fig. 5. The deformation pattern has similar features to those in the 1-m embankment, but it now takes 2 mm of plate subsidence  $\delta$  for the vertical shear band to reach the embankment crown, Fig. 5(g). Shortly after, another shear band propagates from the edge of the cap beam toward upper-right corner of the model, and the vertical displacement increment field is dominated by three displacement zones, Fig. 5(c,h), separated by the two shear bands. The distribution of the vertical displacement increments indicates that the differential settlements propagate to the embankment surface, and the embankment height of 2 m is found to be lower than the critical height (for the parameters used in computations and the column spacing of 2.0 m). At settlement of 20 mm, the mechanism resembles that for the 1-m embankment. The major principal stress trajectories assume a similar shape for both embankments, with the major principal stresses being horizontal at the symmetry plane.

When the embankment height is increased to 3 m, the shape of the major principal stress trajectories and the failure mechanism drastically change, Fig. 6. In the early stages of settlement  $\delta$ , a vertical shear band propagates upward from the edge of the cap beam, Fig. 6(f,g), but this shear band does not reach the embankment surface. Instead, a characteristic shear band pattern is formed in the lower part of the embankment, resembling an inverted Prandtl-type punch indentation problem (Prandtl, 1920). This mechanism persists throughout the remainder of the 20-mm settlement of the soft soil, and beyond. This pattern of shear zones is quite similar to that in bulk materials flowing through flat-bottom silos with smooth walls (Krzyżanowski et al., 2020). The differential settlements seen distinctly in the lower portion of the embankment fill, Fig. 6(a) through (e), do not reach the embankment surface, indicating that height  $H = 3$  m is larger than critical. It is noted that the shear bands shown in the bottom rows of Figs. (4)–(6), are also indicative of bands of dilation. This is because the shear strains and the volumetric strains are uniquely related to one another through the flow

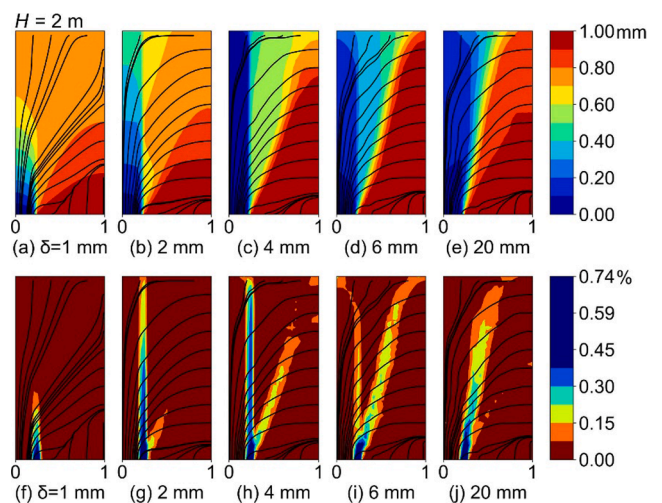


Fig. 5. Embankment with 2-m height at  $\delta = 1, 2, 4, 6,$  and  $20$  mm: (a) – (e) a sequence of vertical displacement increments, and (f) – (j) a sequence of maximum shear strain increments ( $s = 2.0$  m,  $b = 0.4$  m).

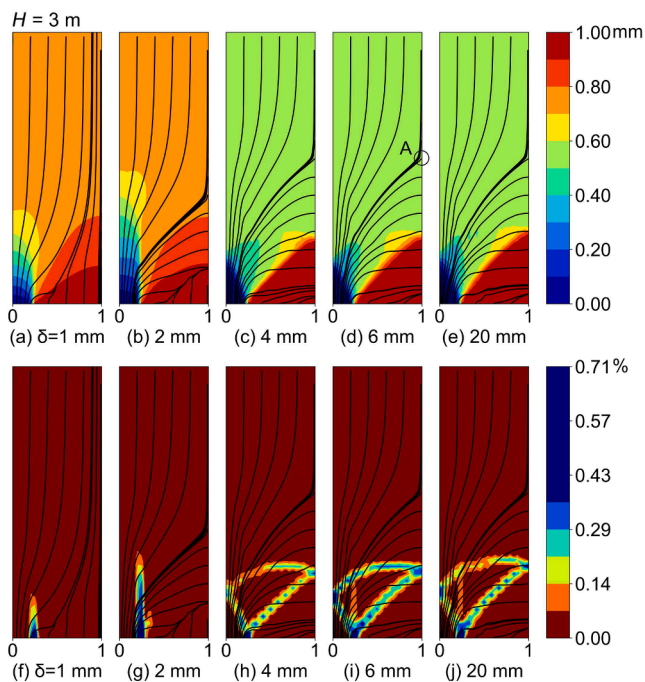


Fig. 6. Embankment with 3-m height at  $\delta = 1, 2, 4, 6,$  and  $20$  mm: (a) – (e) a sequence of vertical displacement increments, and (f) – (j) a sequence of maximum shear strain increments ( $s = 2.0$  m,  $b = 0.4$  m).

rule in Eq. (5).

### 3.3. Diffused arching

An interesting distribution of the major principal stress trajectories was developed early in the settlement process of the 3-m tall embankment. As plotted in Fig. 6(c), the trajectories start vertical from the surface of the capping beam. The ones originating on the right-side of the capping beam divert to the right and terminate at the right boundary, assuming a horizontal direction (forced by the boundary condition). The shape of these trajectories resembles the force chains illustrated in

Fig. 1. The remaining trajectories propagate upward, curve to the right as the other ones did, but do not reach the right boundary; instead, they divert upward, assuming a vertical direction, indicating vertical (major) and horizontal (minor) principal stresses in the upper portion of the embankment. As a result, there is a singular point on the right boundary of the model, marked as A in Fig. 6(d), below which the major principal stress is horizontal, but vertical above that point. A “switch” in principal stress directions is known to occur in silo flow. Upon opening the discharge outlet in storage bins, a rarefaction wave propagates upward (Michalowski, 1987), coinciding with a rotation of principal stress directions by  $90^\circ$ . Approximate calculations based on the Janssen differential slice method reveal a peak and a stress discontinuity in the wall stress distribution, associated with the rotation of the principal directions (see, e.g., Drescher, 1991). Such a stress discontinuity can only occur within a plastic stress field.

It is not clear if the trajectory direction “switch” point A on the right boundary of the model can be related to the intangible concept of soil arching. In an efficiently designed architectural arch, one would expect little or no bending moments. For the same reason, one might expect a soil arch to form along the trajectories of the major principal stress. However, the fact that these trajectories happen to have an arch-like shape below the “switch” point is not in itself evidence that a soil arch has formed. To shed more light on possible formation of a soil arch, a stress distribution on the vertical boundaries of the computational model are plotted in Fig. 7 for embankments with 2, 3 and 4-m heights.

The distribution of the horizontal stress above the center of the capping beam (left vertical boundary of the model) is increasing with depth, for all three embankment heights, with an increasing gradient. This is not surprising, since the columns attract a considerable portion of the embankment load. However, there is a qualitatively large difference in the stress distribution for the 2-m embankment and the 3- and 4-m embankments on the right-hand side boundary of the model. The stress in the 2-m model increases from the stress-free boundary and becomes close to uniform, before it reduces slightly in the lower portion of the model. For the 3- and 4-m embankments the stress increases nonlinearly with depth until it reaches a maximum, and subsequently sharply declines to reach a minimum in the neighborhood of the point where two shear bands in the failure mechanism approach the boundary, Fig. 7(b,c).

If a distinct soil arch was formed, one would expect some disturbance

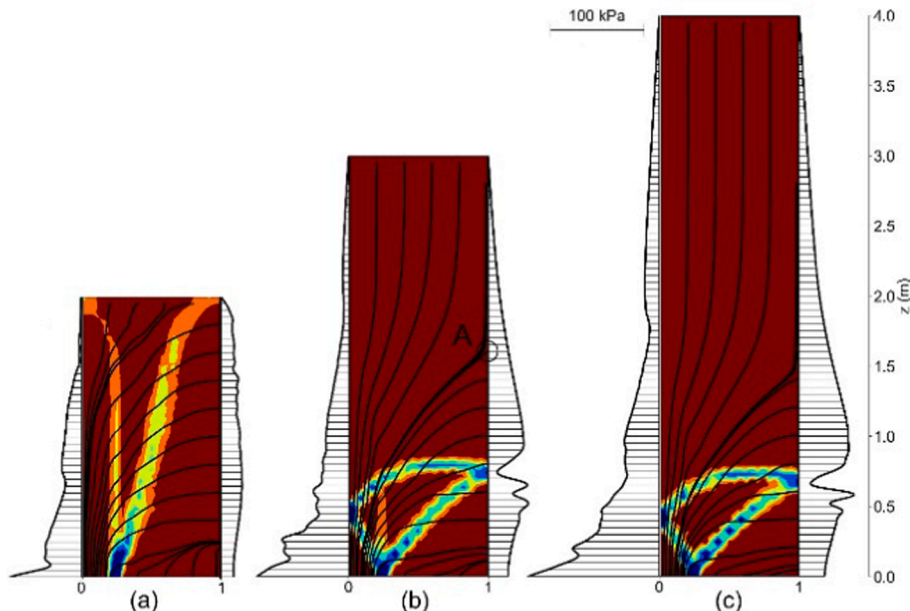


Fig. 7. Distribution of horizontal stresses on vertical boundaries of the model for embankments with 2, 3 and 4-m height.

in the stress distribution, possibly a sharp increase in stress, but the distribution is smooth when passing point A (switch point), and continues increasing until reaching the maximum above the failure mechanism that developed in the lower portion of the embankment. To gain a better understanding of the stress state in the neighborhood of point A, a distribution of the minor-to-major principal stress ratio was plotted in Fig. 8(a). It follows from the Mohr-Coulomb failure criterion that for a material with  $\phi = 40^\circ$ , ratio  $\sigma_3/\sigma_1$  is approximately 0.217 at the plastic stress state; because  $\sigma_3 \leq \sigma_1$ , this ratio cannot exceed one.

The color scale in Fig. 8(a) reveals that the stress state at point A is isotropic ( $\sigma_3/\sigma_1 = 1$ ). The stress state at point A is elastic, and the point is not the kind encountered in silo flow mentioned earlier in this subsection. The isotropy of the stress state at point A is something of a peculiarity. Now, this point should more appropriately be called an isotropic stress point, rather than a “switch point.” It is interesting to notice that the stress state is isotropic also at a point close to the lower right corner of the computational model. Approximately the upper-right quadrant of the modeled portion of the embankment is in the elastic state. The lower region where the failure mechanism has developed is in the plastic state with neighboring zones in the near-plastic range (with an exception of the lower-right corner). The shear strain increments are the largest within the shear bands (Fig. 7(b)), but the plastic stress state also covers the area between the shear bands where the distributed (as opposed to localized) plastic deformation takes place. The left side of the model, up to about two-thirds of the height, is in the plastic or near-plastic state.

The formation of a distinct soil arch was not detected, although the major principal stress trajectories below isotropic stress point A appear to have an arch-like shape. The plot of the minor-to-major principal stress ratio distribution,  $\sigma_3/\sigma_1$ , is presented in Fig. 8(a), which indicates the proximity of the stress to the plastic stress state, but this plot does not indicate the magnitude of stresses. The limit state is reached when ratio  $\sigma_3/\sigma_1$  reaches the minimum value of 0.217, and it is depicted in dark blue, whereas the isotropic stress state is reached when  $\sigma_3/\sigma_1 = 1$  (dark red). To reveal information about the stress magnitude, the in-plane mean stress,  $(\sigma_1 + \sigma_3)/2$ , is plotted in Fig. 8(b). The mean stress reaches a high magnitude immediately above the cap beam (up to 161.9 kPa); therefore, the color scale was not extended to that region (hashed area) in order to preserve a higher resolution of the scale in the range up to 50 kPa. The plot shows a region immediately beneath the isotropic stress point A (light green), in which the mean stress is larger than the stress above or below. One might propose a hypothesis of a *diffused* soil arch, which extends from the right boundary of the model, somewhere from that region of the elevated mean stress, toward the cap beam

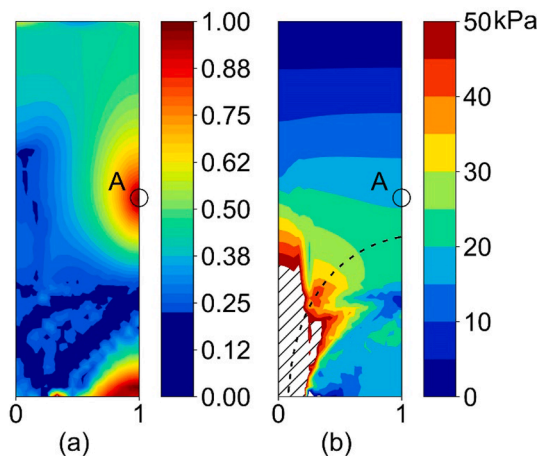


Fig. 8. Stress field characteristics in 3-m high embankment: (a) plot of the minor-to-major principal stress ratio  $\sigma_3/\sigma_1$ , and (b) distribution of in-plane mean stress  $(\sigma_1 + \sigma_3)/2$ .

support in the lower-left corner of the model, approximately along the major principal stress trajectories (Fig. 7(b)). The black dashed line in Fig. 8(b) is what might be approximately the center line of the hypothetical diffused arch.

Fig. 9 shows horizontal stress distribution  $\sigma_{xx}$  on the right-side boundary of the 3-m embankment model (solid line), superimposed on the initial elastic distribution (dotted line) and the mean stress along that boundary. The distributions of the boundary stress  $\sigma_{xx}$  and the in-plane mean stress are shown at the instant when the bottom plate reached a displacement of 6 mm. The boundary conditions require stress  $\sigma_{xx}$  to be equal to either the major or the minor principal stress in the embankment fill along the boundary. Stress  $\sigma_{xx}$  is increasing nonlinearly with depth, with a maximum at about  $z = 0.9$  m; this distribution might be indicative of the presence of a diffused soil arch. The contours of the arch are not defined by any distinct characteristics, hence the term *diffused* arch. For lack of a better definition of arch geometry, it is suggested that the presumed arch meets the right-side boundary of the model somewhere between the isotropic stress point (at the elevation of about 1.6 m in this example) and slightly past the first maximum in the stress distribution (about 0.8 m). This range is shaded in Fig. 9.

The fluctuation of the horizontal stress below the shaded range in Fig. 9 is surprising, but it is consistent with the fluctuation of the in-plane mean stress. The stress state is isotropic at the two points where stress  $\sigma_{xx}$  is equal to the mean stress; both points are clearly identifiable in Fig. 8(a). Principal stress directions rotate by  $90^\circ$  at both points, but the model is not refined enough to show the detailed trajectories in the neighborhood of the lower isotropic point. Boundary stress  $\sigma_{xx}$  between the two points is equal to the major principal stress in the soil along that boundary, and it is equal to the minor principal stress above and below that range. One can easily show that in the limit state for soil with  $\phi = 40^\circ$ , the ratio of the mean stress to the major principal stress is about 0.61, and the range of soil in the plastic state can be identified right below the shaded area in Fig. 9.

A periodic cell between two neighboring columns spaced by distance  $s$  is illustrated in Fig. 10(a). The color scale illustrates vertical displacement increments at settlement  $\delta = 6.0$  mm. The apparent diffused soil arch is formed below the isotropic stress point A, presumably following the trajectories of major principal stresses, with firm support on the capping beams. A triangular region in the lower part of the embankment appears to move down approximately as a rigid body, but the differential settlements clearly illustrated at the bottom of the

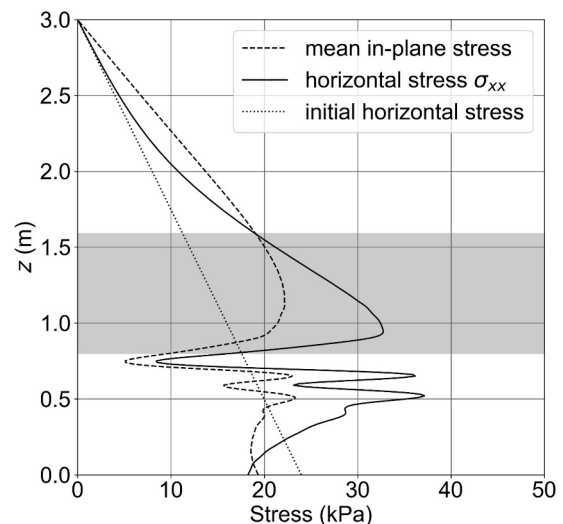


Fig. 9. An increase in the horizontal stress on the right boundary of the computational model (symmetry plane of the cell in Fig. 10), associated with a hypothetical diffused soil arch.

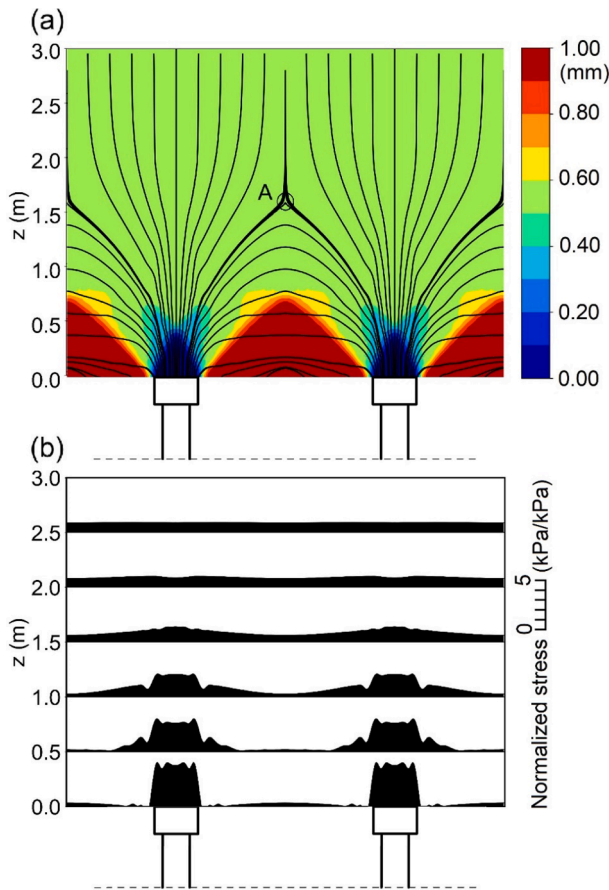


Fig. 10. Full cell between two adjacent columns: (a) vertical displacement increments with distribution of the major principal stress trajectories, and (b) distribution of normalized vertical stresses in the embankment fill.

embankment do not propagate upward to the embankment surface. The distribution of vertical stresses on horizontal planes at half-meter intervals is illustrated in Fig. 10(b). The stresses were normalized by the average vertical stress  $[\rho g(H - z), g - \text{gravity acceleration}]$ , so their integral is the same at every depth.

For both 3- and 4-m embankments, the presumed diffused soil arch passes through the failure mechanism. However, the vertical displacement increments illustrated in Fig. 6(d) indicate nearly uniform settlement on the path of the major principal stress trajectories, and thus the

diffused arch in that region (also illustrated in Fig. 10(a)).

Formation of the fields of displacement increments and maximum shear strain increments were illustrated in Figs. 4–6. Results of calculations were shown for soft soil settlement  $\delta$  up to 20 mm, but for some examples, calculations were carried out up to 100 mm, without noticeable change to the distribution of the vertical displacement or the maximum shear strain increments. Fig. 11 illustrates the respective increments for embankment heights from 1 to 5 m, at soft soil settlement  $\delta = 6$  mm. The comparison indicates that the increase in the height beyond 3 m results in a qualitatively very similar field of vertical displacement increments, the failure mechanism, and the trajectories of major principal stresses. It is noticed that the location of the isotropic stress point moves down with an increase in the embankment height and so does the failure mechanism limited by the upper shear band. This conclusion is made for this particular geometry of the column support system and material properties, but the same qualitative trend is expected to hold for a wider range of geometry and material properties.

#### 4. Critical height and efficacy

Critical height and efficacy are numbers of importance in design of pile-support systems for embankments on soft soils. Both are discussed in the following subsections.

##### 4.1. Critical height

Critical height  $H_{crit}$  was already defined as the minimum embankment height when the differential settlements no longer propagate to the embankment crown. The critical height is a function of both the geometry of the support system and the material properties of the embankment soil. It is evident from Fig. 11(a) that the embankment critical height for this particular column spacing and material properties of the fill is between 2 and 3 m.

Fig. 12(a) shows the differential settlements as a function of embankment height. Differential settlements are calculated as a difference in settlement at the same elevation between two points, one directly above the mid-point between two neighboring rows of columns (right edge of the model) and one above the center of the cap beam (left edge of the model). It is evident from Fig. 12(a) that for a 2-m embankment, the differential settlements (not total settlements) at the crown are 10 mm, but at the elevation of 1.5 m they are almost 15 mm. The differential settlement drops to nearly zero (0.12 mm) at the crown level when the embankment reaches a height of about 2.2 m, and zero when  $H = 2.3$  m. It is emphasized that these results are valid only for the considered geometry of the support system ( $s = 2.0$  m,  $b = 0.4$  m) and the properties in Table 1. However, it is not a coincidence that an

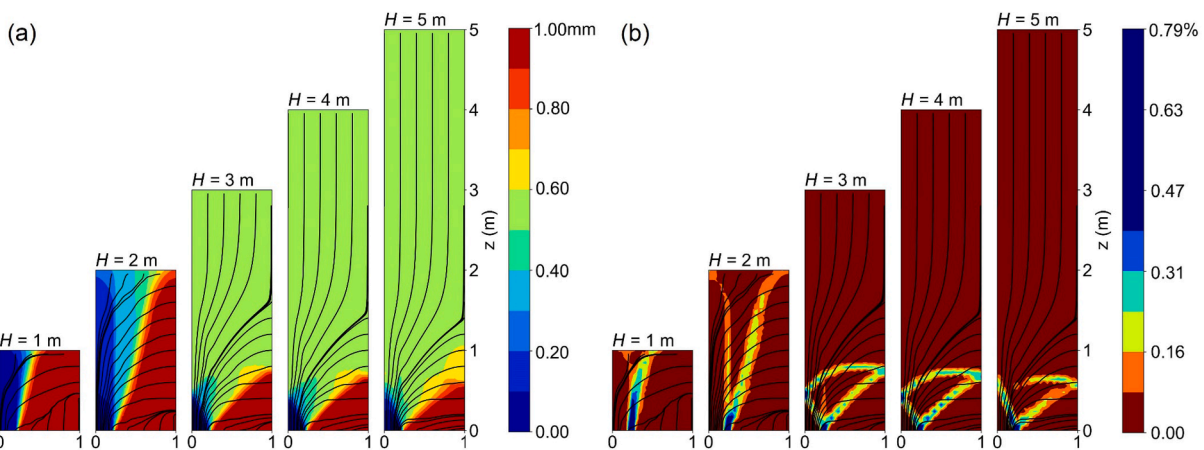


Fig. 11. Results for embankments of 1–5 m height at  $\delta = 6.0$  mm: (a) comparison of vertical displacement increments, and (b) comparison of maximum shear strain increments.

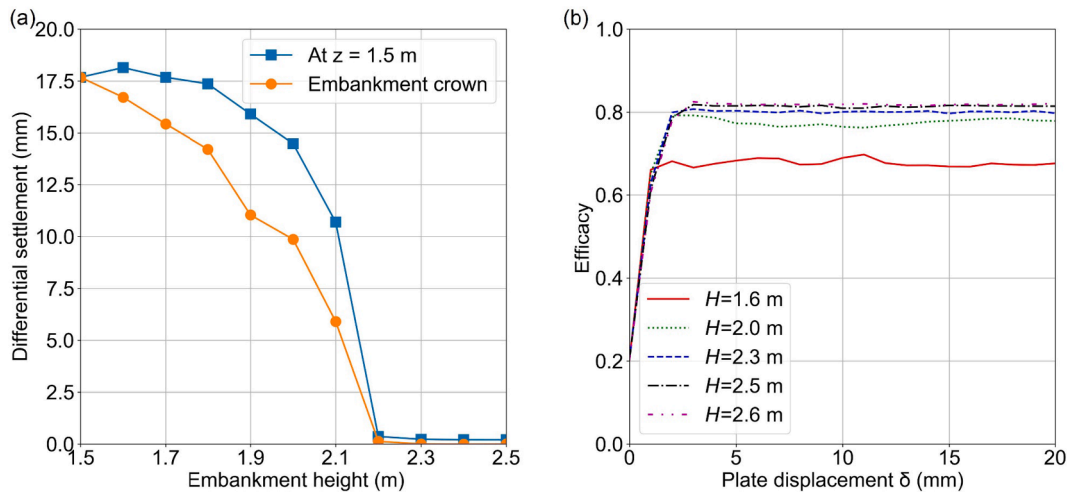


Fig. 12. Differential settlement and efficacy for embankments of height lower and larger than critical height: (a) differential settlement at  $z = 1.5$  m and at the embankment crown when plate displacement  $\delta$  reached 20 mm, and (b) increase in efficacy as a function of plate displacement  $\delta$ .

empirical formula cited by Filz et al. (2012) applied to this example yields the critical height of 2.29 m (notice the different use of symbols).

To indicate the sensitivity of the critical height to the stiffness of the embankment fill ( $E$ ), internal friction angle ( $\phi$ ), and dilatancy angle ( $\psi$ ) a set of computations was carried out, first with the parameters as in

Table 1, and then with one of the three parameters modified to a different value. The outcome of these computations is illustrated in Fig. 13, with the specific material parameters indicated in the legend for each chart. While the large dilatancy angle considered for the case in Fig. 13(d) is not realistic for sand, it is interesting to see the tendency of

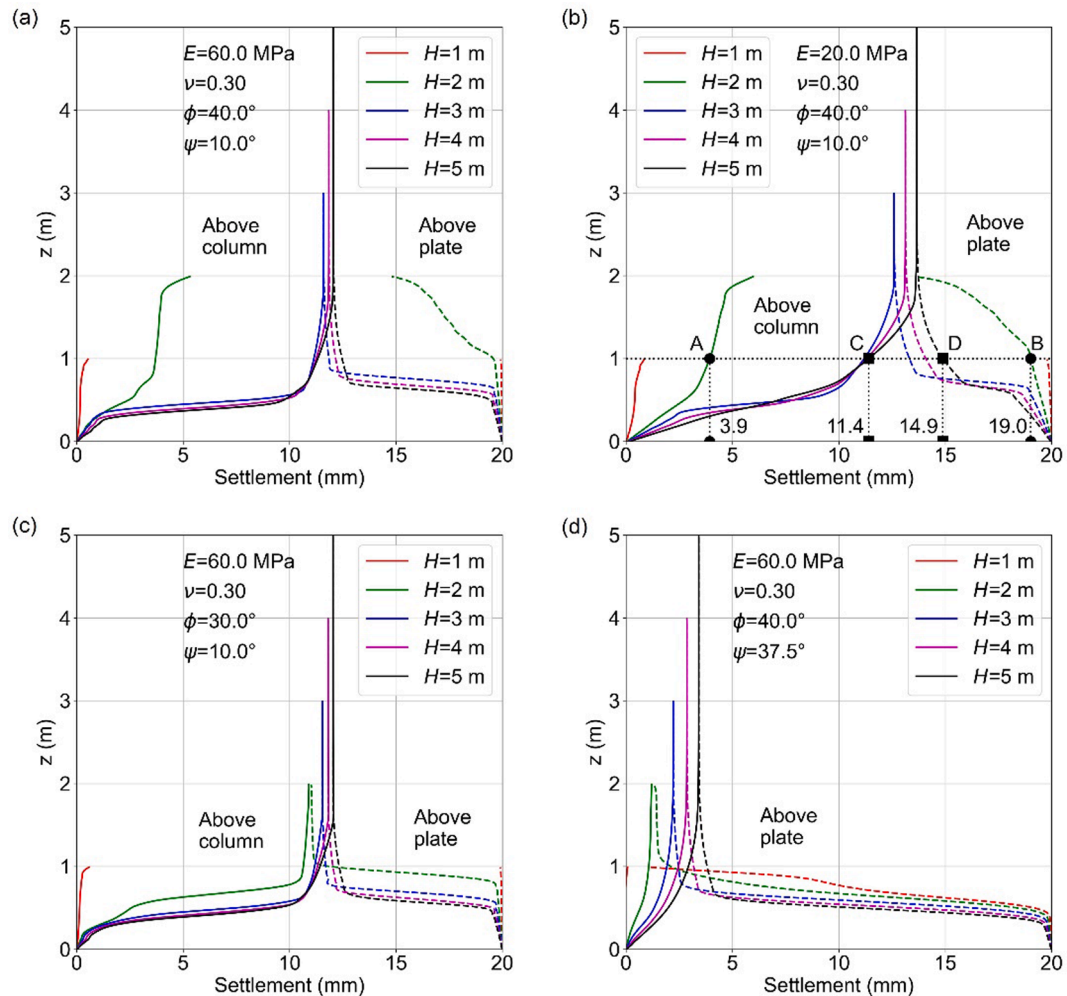


Fig. 13. Settlements throughout the embankment above the capping beam center (solid lines) and above the soft soil (plate center) for four sets of parameters ( $s = 2.0$  m,  $b = 0.4$  m).



the solution when the nearly associative plastic flow rule is used in the material description. All results in Fig. 13 were obtained from calculations with column spacing of  $s = 2$  m, capping beam width  $b$  of 0.4 m, and a soft soil settlement of 20 mm. However, further simulations with settlement of up to 100 mm revealed no influence on the critical height of the embankment.

All graphs in Fig. 13 show the settlements at elevations  $z$  above the center of the column (solid lines) and above the mid-point between two rows of the columns (dashed lines) for embankments with a height from 1.0 to 5.0 m, when the settlement of the soft soil ( $\delta$ ) reached 20 mm. The “spread” of the solid and dashed lines for an embankment of given height indicates the differential settlement at varied elevations. For example, the difference in settlement indicated by points A and B in Fig. 13(b) indicates a 15.1 mm of differential settlement in a 2-m tall embankment at an elevation of 1 m ( $19.0 - 3.9 = 15.1$  mm). At the crown of the 2-m embankment, the two terminal points are still about 7.5 mm apart, indicating that the critical height is larger than 2.0 m. For a 5-m embankment, the differential settlement at an elevation of 1.0 m is 3.5 mm, and it is defined by the spread of points C and D. The two curves join at the elevation slightly above 2.0 m, and no differential settlement is present at higher elevations. The 5-m (as well as the 3.0 and 4.0 m) embankment is higher than the critical height.

For the “standard” set of parameters in Table 1 and the one with a reduced Young’s modulus from 60 to 20 MPa, the 2-m tall embankment displays a substantial differential settlement at the crown level, Fig. 13(a,b). However, if the internal friction angle is decreased from  $40^\circ$  to  $30^\circ$ , or if the dilatancy angle is increased from  $10^\circ$  to  $37.5^\circ$ , the differential settlements at the embankment surface are reduced to nearly nil, Fig. 13(c, d). This is a consequence of the influence of the internal friction angle and the dilatancy angle on the failure mechanism. To demonstrate this influence, vertical displacement increments and the shear strain increments are presented in Fig. 14 from simulations of a 2-m tall embankment with different sets of parameters. The top row of graphs, (a) through (c), shows the distribution of the vertical displacement increments when the settlement increment of the soft soil was 1 mm and the total settlement of the soft soil reached 6 mm. The lower row, (d) through (f), shows the respective shear strain increments. For the standard set of parameters, Fig. 14(a,d), a distinct shear band forms

from the edge of the cap beam to the top boundary, and the displacement increment at the embankment crown (top boundary) is not uniform, indicating differential settlements. The height of the embankment has not reached its critical value yet.

However, the deformation pattern (for the same embankment height) changes significantly when the internal friction of the soil is reduced from  $40^\circ$  to  $30^\circ$ , Fig. 14(b,e). The position of the localized shear zones is now limited to the lower part of the embankment, producing no differential settlement at the crown, even though there is a substantial variation in the field of vertical displacement increments in the lower portion of the embankment. The pattern of the localized shear zones in this case resembles that in the taller embankments with a standard set of parameters, Fig. 11. If the dilatancy angle of the fill is increased from  $10^\circ$  to  $37.5^\circ$ , the deformation field is characterized by one distinct shear band, Fig. 14(f). This band separates a triangular block in the lower-right moving downward from the field above, characterized by substantially lower displacement increments, no localized strain, and displaying no differential settlements at the embankment crown, Fig. 14(c). The large difference in the magnitude of the displacement increments in the two fields can be attributed to a large volumetric strain in the shear band. The graphs in Fig. 14 indicate clearly that it is not only the geometry of the system (embankment height relative to the column spacing), but also the material properties that play an important role in defining the embankment critical height.

#### 4.2. Efficacy

Efficacy  $E_f$  of the column support system is defined as the fraction of the embankment load carried by the pile/column support system, and for the system with cap beams (2D), it can be expressed as

$$E_f = \frac{2 \int_0^{b/2} \sigma_{zz} dx}{\rho g s H} \quad (9)$$

where  $s$ ,  $b$  and  $H$  are the column spacing, cap beam width, and the embankment height, respectively (Fig. 3);  $\rho g$  is the unit weight of the embankment fill, and  $\sigma_{zz}$  is the vertical stress on the capping beam. Essentially, the numerator represents the load transmitted to the cap beam while the denominator is the total embankment weight (load) in the periodic cell. The actual calculations of efficacy did not follow the definition in Eq. (9) exactly. Because the capping beam and the soft soil surface were both modelled as rigid plates, use was made of the reactions calculated in the Abaqus analysis. The vertical component of the resultant reaction of the plate simulating the cap beam,  $R_1$ , is equal in magnitude to the numerator in Eq. (9), whereas the denominator is equal to the sum of  $R_1$  and vertical reaction  $R_2$  of the second rigid plate. Consequently, the efficacy was calculated as  $R_1/(R_1 + R_2)$ .

The efficacy is dependent on the geometry of the pile support system and the material properties of the fill, and it requires some settlement of the soft soil beneath the embankment before it can reach its full value. Fig. 12(b) shows the development of efficacy in relation to reaching the critical height. The 1.6-m embankment has not reached the critical height (Fig. 12(a)), and its efficacy reaches a maximum value of about 0.68 (Fig. 12(b)), but the efficacy increases to about 0.77 for a 2-m embankment, even though both are below the critical height. Once the height of the embankment reached the critical height at about 2.3 m (Fig. 12(a)), the efficacy stabilized at about 0.80, and marginally increases to 0.82 for a 2.6-m embankment.

The efficacy increases with an increase of the embankment height as shown in Fig. 15(a). It takes a larger settlement to reach full efficacy for taller embankments, as evident in all charts in Fig. 15. For the standard set of parameters (Table 1), the efficacy of a 5-m embankment reaches a plateau at about 0.88. A low embankment of 1-m height has a low efficacy of about 0.54, Fig. 15(a). These results are reported in the third column of Table 2. The deformation process in such a low embankment is dominated by the failure mechanism.

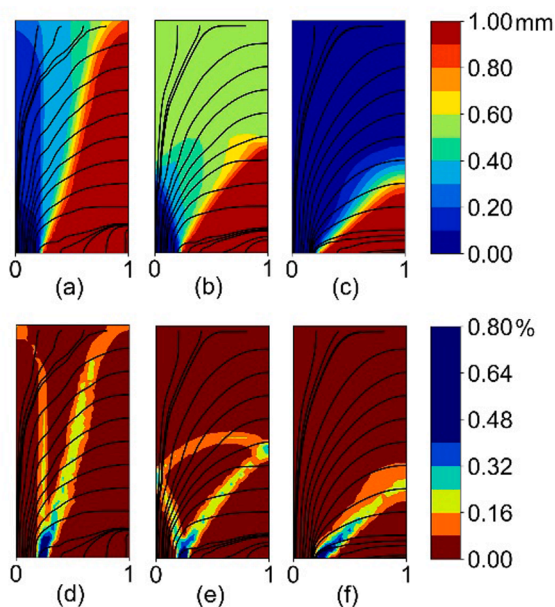


Fig. 14. Comparison of results for 2-m tall embankments; upper row: increments of vertical displacements; lower row: shear strain increments, (a) and (d) parameters as in Table 1, (b) and (e)  $\phi = 30^\circ$ , all other parameters as in Table 1, (c) and (f)  $\psi = 37.5^\circ$ , all other parameters as in Table 1.

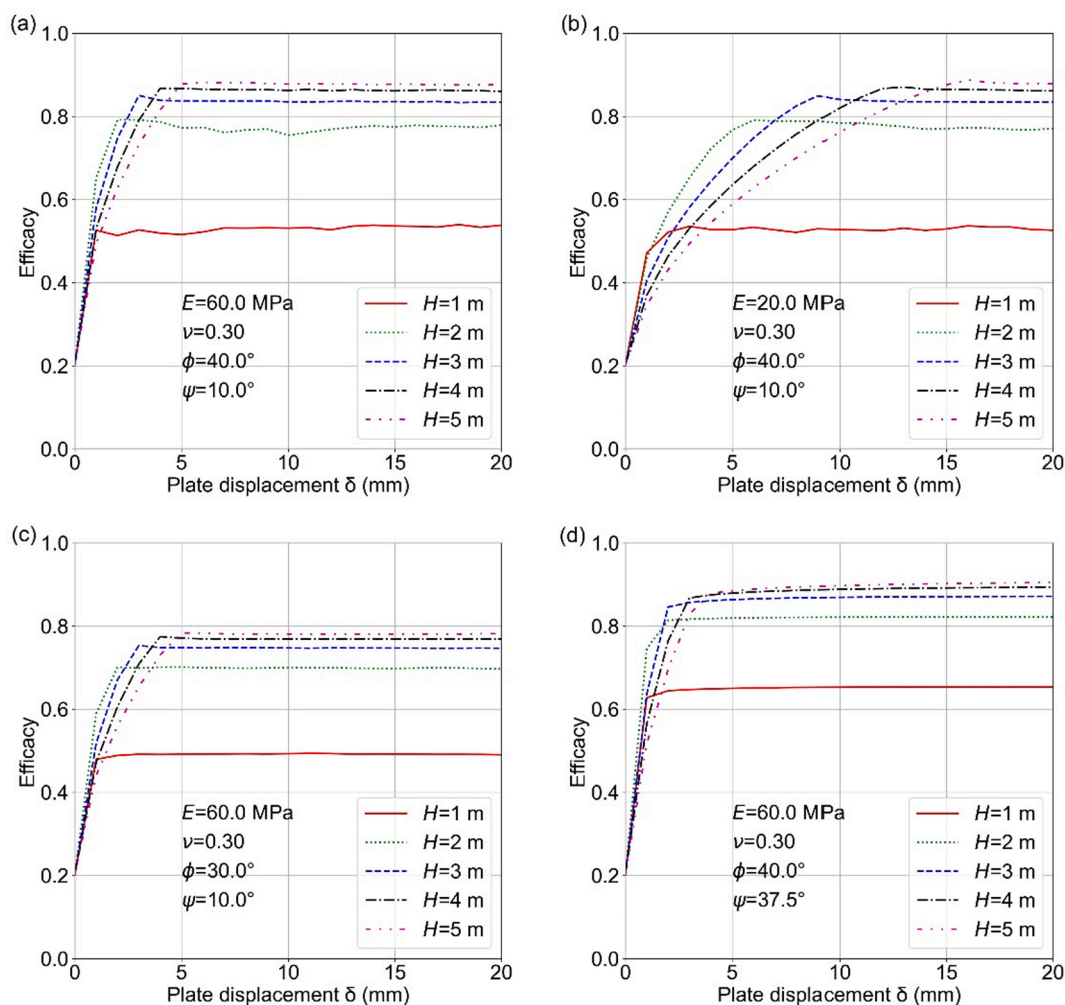


Fig. 15. Mobilization of efficacy with an increase in soft soil settlement for four sets of material properties ( $s = 2.0$  m,  $b = 0.4$  m).

**Table 2**  
Dependence of efficacy on embankment soil parameters.

H (m)	H/s	Properties			
		Properties as in Table 1	$\phi^* 30^\circ$	$E^* 20$ MPa	$\psi^* 37.5^\circ$
1.0	0.5	0.538	0.491	0.526	0.653
2.0	1.0	0.779	0.697	0.771	0.822
3.0	1.5	0.834	0.747	0.834	0.872
4.0	2.0	0.860	0.769	0.862	0.893
5.0	2.5	0.877	0.782	0.879	0.905

\* All other parameters as in Table 1; cap beam width  $b = 0.4$  m.

Although a distinct feature of the 2-m embankment is also the failure mechanism with no diffused arch formation, the efficacy is substantially higher at about 0.78. If the strength of the fill remains the same, but the soil becomes softer in the elastic range, the efficacy is not affected, but it takes a considerably larger settlement to reach it, Fig. 15(b). For example, reducing the Young’s modulus three-fold (from 60 to 20 MPa) for a 5-m embankment requires an increase from 5 to 15 mm of soft soil settlement to reach the full value of efficacy. It does not come as a surprise that the efficacy increases with an increase in dilatancy angle 15 (d), and it decreases if the internal friction angle is reduced 15(c). These results are reported in Table 2. The data is reported with three digits after the decimal point for comparative reasons only, and not to suggest that the model provides such a high accuracy.

Calculations using the conventional displacement-based FEM

without regularization revealed a small dependence of efficacy on the mesh size. For example, the efficacy of a 3-m tall embankment (parameters in Table 1) dropped by 0.6% when the number of nodal points in the model was increased from 1600 to 2700, and this drop in efficacy had a tendency to asymptotically decrease with a further increase in the number of nodes in the mesh. Representing the efficacy as a function of the reciprocal of the number of nodal points revealed that the asymptotic value was within about 1% of the efficacy calculated.

The outcome of calculations is affected by the geometry of the system, i.e., by the ratio of the embankment height to the column spacing, and by the ratio of the area covered by the capping beams to the area of the periodic cell (in this 2-D analysis equal to  $b/s$ ). The data reported thus far comes from calculations with  $b/s = 0.2$ . Additional results for ratios 0.1 and 0.4 are given in Table 3. Not surprisingly, efficacy increases with an increase in ratio  $b/s$ .

**Table 3**  
Dependence of efficacy on the width of the capping beam.\*

H (m)	H/s	b/s		
		0.1	0.2	0.4
1.0	0.5	0.449	0.538	0.746
2.0	1.0	0.726	0.779	0.886
3.0	1.5	0.777	0.834	0.918
4.0	2.0	0.799	0.860	0.937
5.0	2.5	0.814	0.877	0.948

\* Soil properties as in Table 1.

Simulations of efficacy were carried out assuming an instantaneous embankment construction, which is a significant approximation of the staged construction process. To assess the influence of this approximation on the magnitude of efficacy calculated, the development of efficacy during a staged, 5-layer embankment construction, was simulated for a 3-m tall embankment with material properties as in Table 1. An increase in efficacy during the staged construction process is illustrated in Fig. 16 as a function of the soft soil settlement, based on the results of the simulation.

The initial (minimum) efficacy is defined here as the ratio of the area of the capping beams to the area of the periodic cell of the pile support system, Fig. 3. Because spacing  $s$  of the columns in this simulation was 2.0 m and cap beam width  $b$  was 0.4 m, the area ratio is  $b/s = 0.2$ . The load of each of the five layers of the embankment fill is applied instantly. The first layer load application takes place at efficacy of 0.2, point A in Fig. 16. Subsequently, as the soft soil settles, the efficacy increases to reach point B. Once the load of the second layer is applied, the efficacy drops by some amount to reach point C. This is because the load of the layer is applied instantly and uniformly across the periodic cell. Although the settlement of the soft layer is modeled as the boundary displacement, the nature of this displacement is owed to the consolidation process of the soft soil, hence there is no immediate settlement at the instant of load application. However, the efficacy increases to reach point D, as the settlement of the soft soil subsequently takes place. This cycle is then repeated for the three subsequent layers to reach the maximum efficacy of 0.847 at point E. The efficacy then stabilized at the level of 0.835 after a total of 10 mm of settlement. The efficacy calculated assuming instant loading from the entire embankment was 0.834 (Table 2). While instant loading from the entire embankment may seem a crude assumption, it does not seem to have a substantial effect on calculated efficacy of the pile support system.

## 5. Final remarks

An analysis of the development of a displacement field and the failure mechanism in column-supported embankments is described in the paper. All conclusions are based on the results of numerical simulations. The problem modeled included columns with parallel capping beams in one direction; hence, it was formulated as a plane-strain problem. In low embankments with a height comparable to the column spacing, or lower, the displacement field was found to be dominated by the failure mechanism with shear bands propagating to the embankment crown, causing differential settlements at the surface. In higher embankments, the failure mechanism resembles an inverted Prandtl-type pattern and it is confined to the lower portion of the fill. Consequently, even though the differential settlements occur at lower elevations within the embankment, they do not propagate to the embankment surface.

The smallest height at which the differential settlements do not reach the embankment crown is referred to as the critical height. This critical height depends very much on the column spacing, but it also depends on the embankment fill properties and the width of the capping beams.

For the specific set of soil parameters and column spacing of  $s = 2.0$  m (and cap beam width of 0.4 m), the critical embankment height was found to be about 2.2–2.3 m, consistent with empirical data found in the literature (Filz et al., 2012). At that embankment height, the efficacy of the system was 0.80. An increase of the embankment height to 5.0 m resulted in an increase in efficacy to about 0.88. Reaching the full efficacy of the system requires some amount of settlement, which was found to be relatively small (millimeters) for the standard set of material properties (Table 1).

Many design recommendations are based on an assumption that a distinct soil arch forms within the embankment fill, aiding in load transfer to the column support. No features in the stress field were found that would indicate clear contours of a distinct soil arch, but a formation of a hypothetical *diffused* arch is suggested in embankments with a

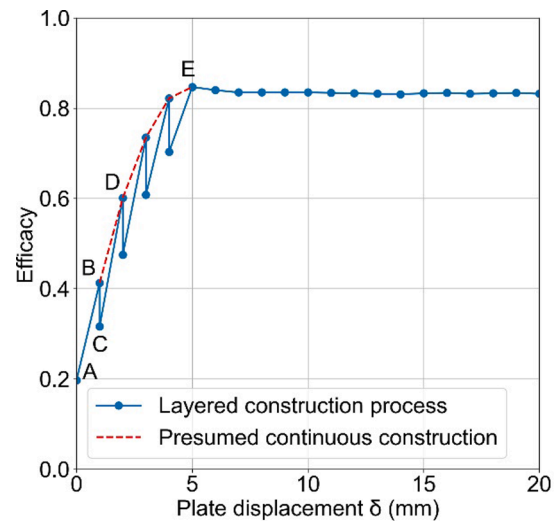


Fig. 16. Development of efficacy during 5-layer construction of a 3-m tall embankment as a function of soft soil settlement.

height larger than critical. As the elastic–plastic stress field develops in early stages of soft soil settlement, a peculiar point on the symmetry plane between neighboring rows of columns was detected, where the principal stress directions rotate by  $90^\circ$ . Upon closer examination, the stress field at that point was found to be elastic and the stress state isotropic. The second point with the isotropic stress state was found in the lower part of the model.

The horizontal stress along the symmetry plane through an individual column-embankment cell was found to be increasing nonlinearly with depth to reach a maximum just above the shear bands in the failure mechanism in the lower portion of the embankment. It is contemplated that the increase in the stress might be associated with the formation of a *diffused* soil arch, which passes the symmetry plane somewhere between the upper isotropic stress point and the proximity of the failure mechanism (Fig. 9).

Much of the current developments in design of piled embankments focus on the use of simplified analytical tools. The use of finite element analysis enabled the authors to focus on the stress field developing in the process of the embankment settlement, which allowed for calculations of the system efficacy and critical height without intuitive assumptions used in simplified analytical approaches.

## Declaration of Competing Interest

The authors declare that they have no known competing financial interests or personal relationships that could have appeared to influence the work reported in this paper.

## Acknowledgements

The work presented in this paper was supported by the National Science Foundation, Grant No. CMMI-1901582. While carrying out this research, Dr. Brzeziński was supported by the Dekaban Fund Fellowship, administered by the University of Michigan. The support from both sources is greatly appreciated.

## References

- Abaqus, 2011. Theory Manual, Ver. 6.11. Dassault Systèmes Simulia Corp., Providence, RI, USA, pp.1172.
- Abusharar, S.W., Zheng, J.-J., Chen, B.-G., Yin, J.-H., 2009. A simplified method for analysis of a piled embankment reinforced with geosynthetics. *Geotext. Geomembr.* 27 (1), 39–52.
- Drescher, A., 1991. *Analytical Methods in Bin-Load Analysis*. Elsevier, Amsterdam.

- Filz, G., Sloan, J., McGuire, M.P., Collin, J., Smith, M., 2012. Column-supported embankments: settlement and load transfer. Geotechnical engineering state of the art and practice: keynote lectures from GeoCongress 2012; Reston, VA, 54-77.
- Han, J., Gabr, M., 2002. Numerical analysis of geosynthetic-reinforced and pile-supported earth platforms over soft soil. *J. Geotech. Geoenviron. Eng.* 128 (1), 44-53.
- Hewlett, W.J., Randolph, M.F., 1988. Analysis of piled embankments. *Ground Eng.* 21 (3), 12-18.
- Janssen, H.A., 1895. Versuche über Getreidedruck in Silozellen. *Zeitschrift Verein Deutscher Ingenieure* 39, 1045-1049.
- King, L., Bouazza, A., Dubsy, S., Rowe, R.K., Gniel, J., Bui, H.H., 2019. Kinematics of soil arching in piled embankments. *Géotechnique* 69 (11), 941-958.
- Krzyżanowski, J., Tejchman, J., Solowski, W., Wójcik, M., 2020. Modelling of shear zones during quasi-static granular silo flow using material point method (MPM). *Powder Technol.* 378, 538-560.
- Ladanyi, B., Hoyaux, B., 1969. A study of the trap-door problem in a granular mass. *Can. Geotech. J.* 6 (1), 1-14.
- Low, B., Tang, S., Choa, V., 1994. Arching in piled embankments. *J. Geotech. Eng.-ASCE* 120 (11), 1917-1938.
- Menetrey, P., Willam, K., 1995. Triaxial failure criterion for concrete and its generalization. *ACI Struct. J.* 92 (3), 311-318.
- Michalowski, R.L., 1984. Flow of granular material through a plane hopper. *Powder Technol.* 39 (1), 29-40.
- Michalowski, R.L., 1987. Flow of granular media through a plane parallel/converging bunker. *Chem. Eng. Sci.* 42 (11), 2587-2596.
- Michalowski, R.L., Park, N., 2004. Admissible stress fields and arching in piles of sand. *Géotechnique* 54 (8), 529-538.
- Michalowski, R.L., Wojtasik, A., Duda, A., Florkiewicz, A., Park, D., 2018. Failure and remedy of column-supported embankment: case study. *J. Geotech. Geoenviron. Eng.* 144 (3).
- Nadukuru, S.S., Michalowski, R.L., 2012. Arching in distribution of active load on retaining walls. *J. Geotech. Geoenviron. Eng.* 138 (5), 575-584.
- Poulos, H.G. A method for analyzing piled embankments. *Proc., Proc., 13th South East Asian Geot. Conf.*, 551-556.
- Prandtl, L., 1920. Über die Härte plastischer Körper. *Nachr. Königl. Ges. Wissensch, Göttingen, Mathematisch-physikalische Klasse*, pp. 74-85.
- Reid, W., Buchanan, N., 1984. Bridge approach support piling. *Proc. Conf. on Advances in Piling and Ground Treatment*. Thomas Telford Publishing, London, pp. 267-274.
- Terzaghi, K., 1943. *Theoretical Soil Mechanics*. Wiley, New York.
- Van Eekelen, S., Bezuijen, A., Van Tol, A., 2013. An analytical model for arching in piled embankments. *Geotext. Geomembr.* 39, 78-102.
- Vardoulakis, I., Graf, B., Gudehus, G., 1981. Trap-door problem with dry sand: A statical approach based upon model test kinematics. *Int. J. Numer. Anal. Meth. Geomech.* 5 (1), 57-78.